Optimization and integration of room temperature RF sputtered ICO as TCO layers in high-performance SHJ solar cells

Özkol, Engin; Magalhães, Maria M.R.; Zhao, Yifeng; Cao, Liqi; Perez-Rodriguez, Paula; Kovačević, Katarina; Procel, Paul; Mendes, Manuel João; Zeman, Miro; Isabella, Olindo

DOI
10.1016/j.solmat.2025.113637

Publication date
2025

Document Version
Final published version

Published in
Solar Energy Materials and Solar Cells

Solar Energy Materials & Solar Cells 288 (2025) 113637

Contents lists available at ScienceDirect

Solar Energy Materials and Solar Cells

journal homepage: www.elsevier.com/locate/solmat

Optimization and integration of room temperature RF sputtered ICO as TCO layers in high-performance SHJ solar cells

Engin Özkol [a,*], Maria M.R. Magalhães [b], Yifeng Zhao [a], Liqi Cao [a], Paula Perez-Rodriguez [a], Katarina Kovačević [a], Paul Procel [a], Manuel João Mendes [b], Miro Zeman [a], Olindo Isabella [a]

[a] Photovoltaic Materials and Devices Group, Delft University of Technology, Netherlands
[b] i3N/CENIMAT, Department of Materials Science, NOVA School of Science and Technology and CEMOP/UNINOVA, Campus de Caparica, 2829-516, Caparica, Portugal

ARTICLE INFO

Keywords:
Cerium-doped indium oxide
Transparent conductive oxide
Room temperature RF sputtering
Electron mobility
Silicon heterojunction solar cells
Short circuit current enhancement

ABSTRACT

In this work, we optimize cerium-doped indium oxide – ICO – thin films with respect to sputtering parameters such as oxygen flow, deposition pressure, applied RF power. Optimized 35-nm-thick ICO layer demonstrated a mobility of 44.22 cm^2/Vs, a carrier concentration of $1.65 \times 10^{20}/cm^3$, and a resistivity of 8.56×10^{-4} Ω cm. Application of such layers into front/back contact silicon heterojunction (FBC-SHJ) solar cells enhanced the short-circuit current density (J_{SC}) by 0.67 when compared to SHJ cell endowed with tin-doped indium oxide (ITO), respectively. This enhancement yielded an absolute power conversion efficiency (PCE) improvement of 0.55 %, reaching efficiencies of around 23.6 % for devices with ICO layers.

1. Introduction

The main focus of PV research in academia has always been increasing the power conversion efficiency (PCE) of solar cells. With the recent record of 27.30 % in silicon heterojunction (SHJ) solar cells [1], the gap with the theoretical efficiency limit, which is 29.4 % for single-junction silicon solar cells [2], has been narrowed down. Indeed, there is still *room for improvement*, but expecting a huge boost is highly unlikely. One of the routes to follow for further closing the gap is developing high mobility transparent conductive oxide (TCO) layers, that enable optimum opto-electrical performance [3], such as cerium-, tungsten-, zirconium-doped or hydrogenated indium oxides (ICO, IWO, IZrO, IO:H).

Although indium consumption is one of the main challenges for scaling up TCOs to industrial level and minimized indium or even indium-free layers were considered in the last decade [4–9], ICO has attracted great attention in recent years due to its better opto-electrical properties and room temperature deposition over its ITO counterpart [10].

To further enhance the performance of this layer, hydrogenation of ICO (ICO:H) could be pursued by adding water vapor during the deposition process. In fact, it is reported that hydrogenation of TCO layers leads to higher charge mobility, lower sheet resistance and higher transparency in the visible and near-infrared regions with reduced free-carrier absorption [11–14]. However, hydrogenation remains a challenge due to equipment limitations in our laboratory. With a tool upgrade, an extension to this work could be carried out in the future.

Reactive plasma deposition (RPD) grown ICO(:H) films exhibit remarkable Hall mobilities higher than 130 cm^2/Vs [15–17], which lead to the highest PCEs obtained with RPD such as 24.84 % [18] and the former world record PCE of 26.81 % [19]. Sputtering technique, which is available in most research laboratories' infrastructures and one of the most established methods for mass production of solar cells [20], was also reported to enable ICO films [21,22]. DC sputtering yields in outstanding PCE of 25.26 % [19], while with RF-sputtered of ICO:H films 21.6 % PCE [21] is obtained. The application of this layer onto solar cells is under-represented, although the previous SHJ structure yielding world record efficiency is obtained with RPD-grown ICO layer. That is, the research on device integration is mostly carried out with RPD grown layers, whereas works focussing on RF-sputtered ICO layers are scarce in literature. In this work, we systematically investigate the opto-electrical properties of ICO films deposited via RF sputtering at room temperature and demonstrate PCE above 23.5 % with a clear increase in the optical response of the front/back-contacted SHJ solar cells with respect to standard ITO.

* Corresponding author.
E-mail address: E.Ozkol@tudelft.nl (E. Özkol).

https://doi.org/10.1016/j.solmat.2025.113637
Received 4 November 2024; Received in revised form 1 April 2025; Accepted 8 April 2025
Available online 16 April 2025

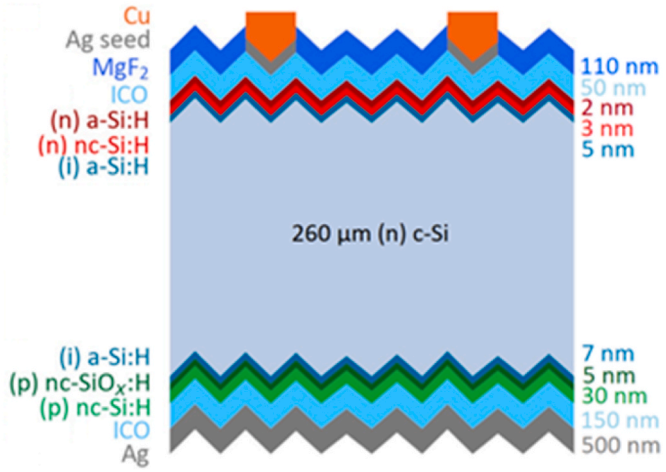

Fig. 1. Manufactured FBC-SHJ solar cell.

2. Experimental

For the material optimization, 35-nm-thick ICO films are sputtered onto Corning Eagle XG glass substrates at room temperature. The sputtering target consists of 97 wt% In_2O_3 and 3 wt% CeO_2. Film thicknesses and average deposition rates are determined via Woollam 2000 spectroscopic ellipsometer.

For opto-electrical properties, four point probe (4 PP) measurements are conducted for sheet resistances. The conductivity (σ), carrier density (N_e), and carrier mobility (μ_e) are determined by the Hall effect measurement system HMS-5000 from ECOPIA CORP. Transmission/reflection data are collected via PerkinElmer Lambda 1050 UV/Vis/NIR spectrometer. Average transmittance is calculated as the integrated area under transmission curve divided by designated wavelength range (300–1200 nm in this case).

For structural analyses, ~200-nm-thick ICO layers are deposited on one-side-polished silicon wafers. SEM measurements are conducted with SEM Hitachi Regulus 8230 at 7 kV with a LA0(UL) detector. Surface morphology is investigated with a Bruker Dimension FastScan A tip AFM with Scanasyst in air mode. Energy Dispersive X-ray (EDX) Analysis is conducted via the Nova NanoSEM 450 at 10 kV of e-beam acceleration voltage.

After material optimization, 50-nm-thick and 150-nm-thick ICO layers are deposited at the front and rear side, respectively, of front/back-contacted (FBC) SHJ solar cells (2 × 2 cm^2 area). While depositing thicker ICO layers, a linear behavior in deposition rate is assumed for adjusting the deposition time. For the textured Si wafer surface, the enlargement area factor is taken as 1.7 [23]. Wafer cleaning procedure and plasma-enhanced chemical vapor deposition growth of silicon layers are explained in details elsewhere [24]. Prior to electroplating, 100-nm-thick Ag seed layer was RF sputtered at room temperature with process parameters of 343 mW/cm^2 applied power, 100 sccm of Ar flux and 5 × 10^{-3} mbar deposition pressure. Copper plating was applied as the front metallization process and a 110-nm-thick MgF_2 layer was e-beam evaporated at the front side forming Double-Layer Anti-Reflecting Coating (DLARC) with TCO layers. Silver was instead thermally evaporated at the rear side. The structure of the cell is shown in Fig. 1 with corresponding layers and thicknesses.

A Sinton Consulting WTC-120 photoconductance decay lifetime tester was used to measure effective minority carrier lifetimes (τ_{eff}) and implied open-circuit voltages (i-V_{OC}) of the cell precursors. In the following, τ_{eff} is reported at an injection level of 1 × 10^{15} cm^{-3}. Current–voltage (*I–V*) characteristics of complete SHJ devices were measured using a class AAA Wacom WXS-90S-L2 solar simulator under 1-sun illumination conditions (100 mW/cm^2, AM 1.5G). In-house external quantum efficiency (EQE) setup was used to obtain the integrated $J_{SC,EQE}$.

3. Results & discussion

3.1. ICO layer optimization

3.1.1. Influence of O_2

In Fig. 2(a), the influence of oxygen (2700 ppm diluted in Ar) addition to a fixed total flow of 20 sccm process gas (Ar) on average transmittance and conductivity is shown. Note that in the optimization sets, the transmission spectrum does not change significantly except for the power series. Therefore, average transmittance is shown instead. Transmission spectra could be found in the Supplementary Information section (see Figs. S1–3). During depositions, pressure and applied RF power are kept constant at 4 × 10^{-3} mbar and 555 mW/cm^2, respectively. Increasing O_2 flow rate from 0 to 9 sccm has slightly increased the average deposition rate from 0.85 to 0.90 nm/min (see Fig. S4). O_2 inclusion lowers oxygen vacancies in the bulk, expected to lead to better transmittance [21]. However, we cannot observe any significant change in transmittance. On the other hand, exceeding 3 sccm flow, the conductivity reduces, which implies O_2 can effectively be incorporated within the bulk. In Fig. 2(b), the influence of O_2 addition to gas mixture on mobility, carrier concentration and resistivity is plotted. Although Hall mobility gets higher with O_2 inclusion, carrier concentration gets lower for which resistivity becomes higher. Considering this trade-off and the lowest resistivity, 3 sccm O_2 flow is set to be the optimal value for the rest of the optimization.

3.1.2. Influence of deposition pressure

The effect of deposition pressure variation under constant O_2 flow (3 sccm) and applied RF power (555 mW/cm^2) is plotted in Fig. 3 (a) for average transmittance and conductivity and in Fig. 3 (b) for mobility, carrier concentration and resistivity. Increasing deposition pressure while keeping the applied power fixed leads to higher residence times of

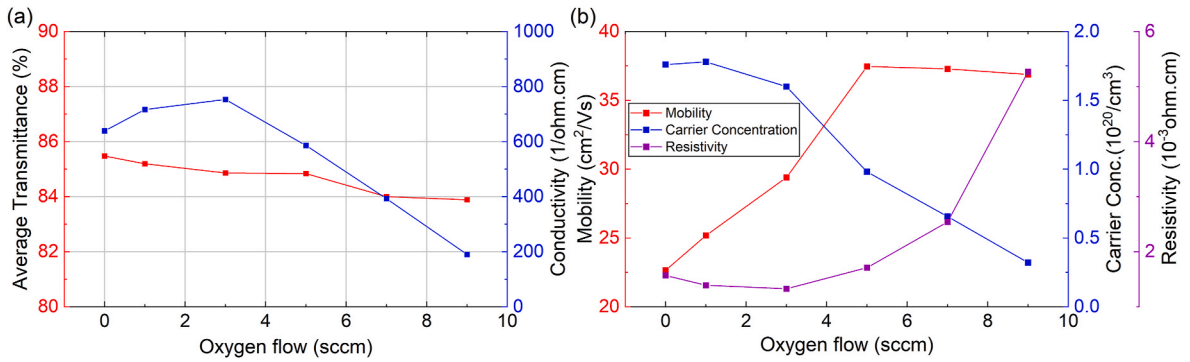

Fig. 2. Influence of O_2 flow on (a) average transmittance and conductivity, (b) Hall mobility, carrier concentration and resistivity.

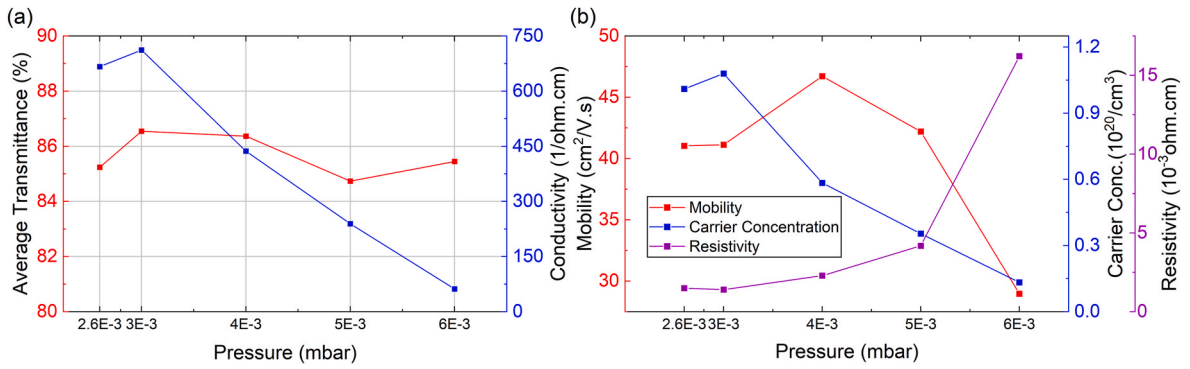

Fig. 3. Influence of deposition pressure on (a) average transmittance and conductivity, (b) Hall mobility, carrier concentration and resistivity.

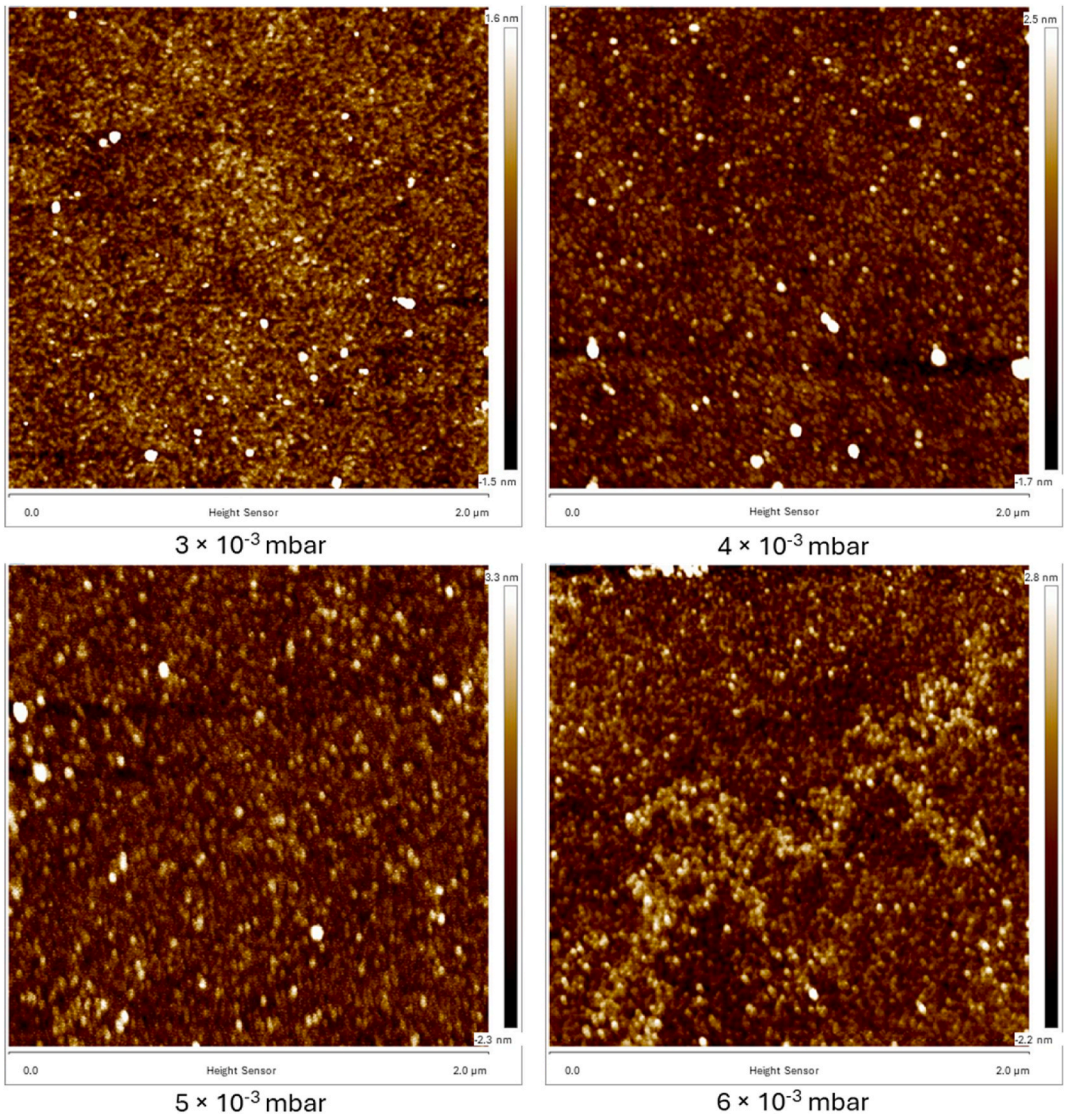

Fig. 4. AFM images for various deposition pressures ranging from 3 to 6 × 10^{-3} mbar. Note that the process parameters other than the deposition pressure are kept constant.

molecules in the chamber and lower ion energy in sputtering process, which causes low sputtering yield and defective structure growth in the bulk (i.e. less crystallinity, different morphological growth) [25,26]. Therefore, resistivity increases whereas both mobility and carrier concentration decrease after exceeding a threshold of 3 × 10^{-3} mbar. However, increasing deposition pressure from 2.6 × 10^{-3} to 6 × 10^{-3} mbar has slightly increased the average deposition rate from 0.82 to 0.86 nm/min (see Fig. S5). AFM images on 35-nm-thick ICO films for different deposition pressure values are shown in Fig. 4. As the morphology hardly changes with deposition pressure, we do not claim

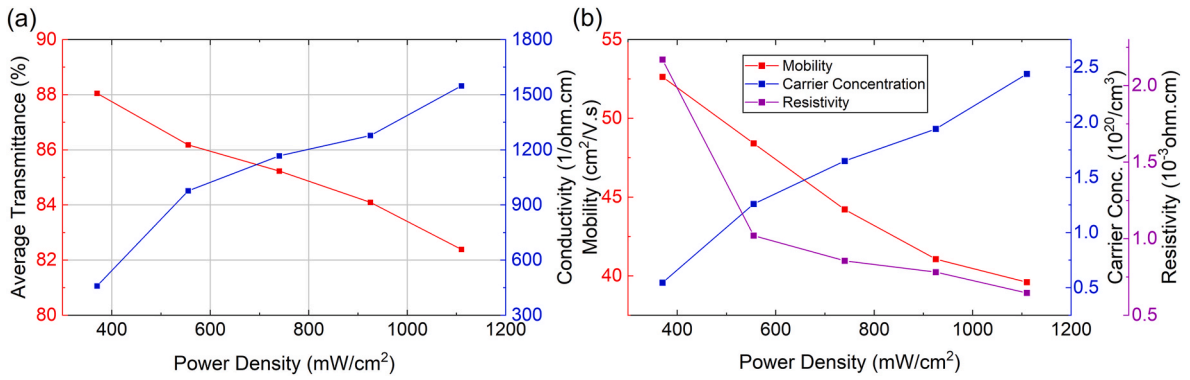

Fig. 5. Influence of applied RF power density on (a) average transmittance and conductivity, (b) Hall mobility, carrier concentration and resistivity.

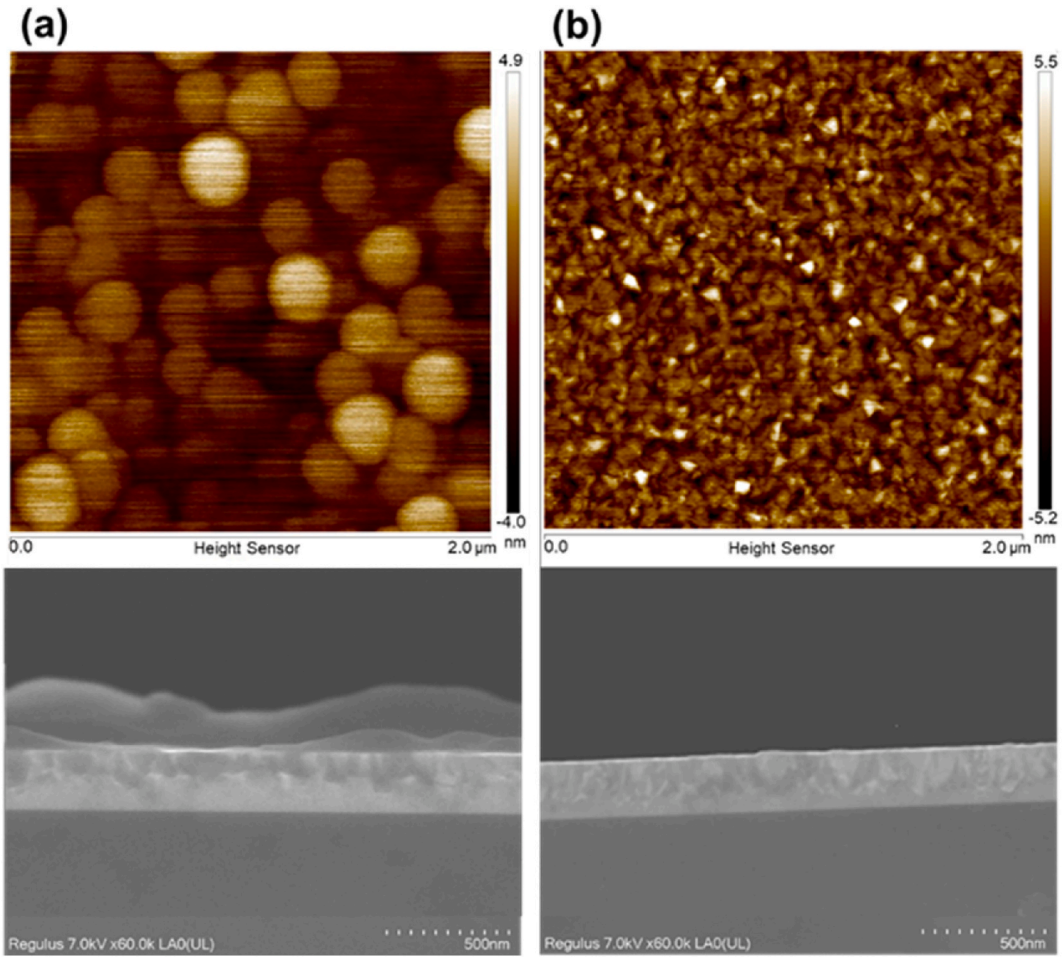

Fig. 6. AFM and SEM images of (a) ICO film deposited at 740 mW/cm^2, (b) ICO film deposited at 925 mW/cm^2, and. Note that the process parameters other than the applied RF power are kept constant.

any morphological growth difference due to pressure. As a conclusion, the optimal pressure value is set to be 3×10^{-3} mbar.

3.1.3. *Influence of applied RF power*

The effect of applied RF power on opto-electrical properties of ICO films is demonstrated in Fig. 5(a) and (b). Increasing the power caused a reduction in average transmittance (also see S3 for transmittance spectra). The possible reason is the increase of the defect density in the bulk at higher power density values. Consequently, grain sizes of the crystallites vary (i.e. smaller volumes) in the bulk [27], which leads to higher conductivity and carrier concentration but lower mobility and transmittance. Increasing the applied power shows almost linear increase in the average deposition rate from 0.62 to 1.86 nm/min (see Fig. S6). To investigate the structural changes, AFM and SEM measurements are conducted. It is observed that the crystalline grains are shrinking in volume as the power density increases (see Fig. 6(a) and (b)). Considering the trade-off between average transmittance and conductivity (see Fig. 6(a)), power is set to be 740 mW/cm^2.

Post-annealing at 180 °C for 5–30 min in ambient atmosphere of the ICO films does not affect any material properties (not shown here), which suggests the bulk is already crystallized during the deposition. According to our results, the main drawback of sputtering over RPD

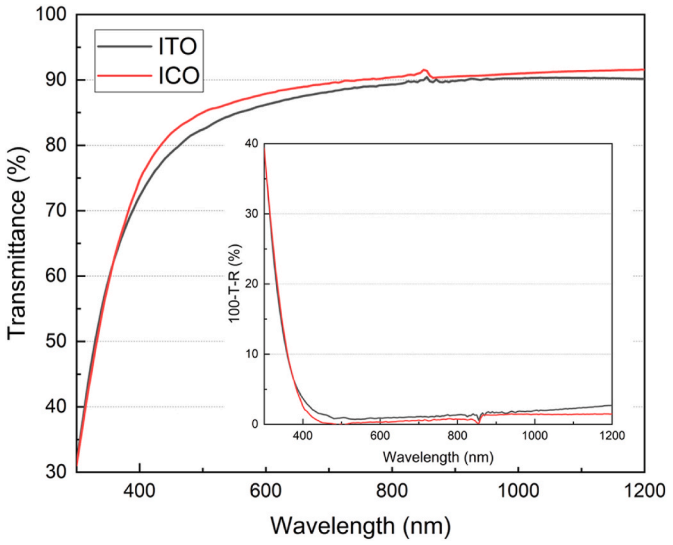

Fig. 7. Comparison of developed ICO and baseline ITO layers in terms of transmittance and absorbance (in the inset diagram).

Table 1
Mobility, carrier density and resistivity of developed ICO(:H) and baseline ITO layers.

	μ (cm^2/Vs)	N (/cm^3)	ρ (Ωcm)
ITO	28.27	1.99×10^{20}	1.11×10^{-3}
ICO	44.22	1.65×10^{20}	8.56×10^{-4}
ICO:H	44.56	1.92×10^{20}	7.28×10^{-4}

technique is the limited size of the crystallites. Therefore the mobility is constrained. With RPD, due to much bigger crystallite sizes, remarkable mobilities could have been achieved [16].

3.1.5. Properties of optimized layers

In Fig. 7, the transmittance and absorbance spectra of 35-nm-thick ICO compared with those of the baseline ITO layers [24] are plotted. ICO layers clearly exhibit higher transparency and lower absorption in the visible and near-infrared regions. It is worth noting the relatively low transmittance within 400–600 nm range is related to non-negligible reflectance of the film and enhanced surface scattering caused by film structure and surface morphology, which causes a drop in optical transmittance [25].

In Table 1, ICO material properties are listed alongside those of the baseline ITO layer. As a result, the optimized 35-nm-thick ICO layer demonstrated a mobility of 44.22 cm^2/Vs.

EDX spectra of the optimized ICO film is shown in Fig. 8 with weight and atomic fractions of the elements. 10 kV acceleration voltage is applied in order to detect the heavy elements. Note that the e-beam penetrates through the film and detects the silicon substrate, which is also included in the inset fraction table. It can be concluded that the films are slightly oxygen rich. We speculate that due to excess oxygen in the films, we could not observe any difference in transmittance during O_2 variation set (see Fig. 2).

3.2. Application of ICO layers on FBC-SHJ solar cells

Subsequent to material optimization, 50 nm front and 150 nm rear ICO layers are sputtered onto baseline cell precursors at room temperature. A reference cell [28] with identical thicknesses of the baseline ITO layers is also manufactured. Following the sputtering process, photoconductance decay lifetime tests are conducted. Initially, the sputtering process caused degradation in the effective minority carrier lifetimes (τ_{eff}) and implied open circuit voltages (i-V_{OC}). Whereas, annealing the precursors under 130 °C in ambient atmosphere for 5 min mostly recovered the τ_{eff} and i-$V_{OC.}$ The results are presented in Fig. S57. The EQE spectra and the calculated $J_{SC,EQE}$ values could be found in Fig. S68.

The 2 × 2 cm^2 sized cells are fabricated onto fully passivated 4-inch round wafers. Thanks to this architecture, there is no significant recombination in the edge regions. During the measurement, the designated cell area (including the metal fingers, excluding surrounding busbar) is illuminated. In Fig. 9, the designated area cell efficiency is reported.

PV external parameters of the FBC-SHJ solar cells endowed with ICO

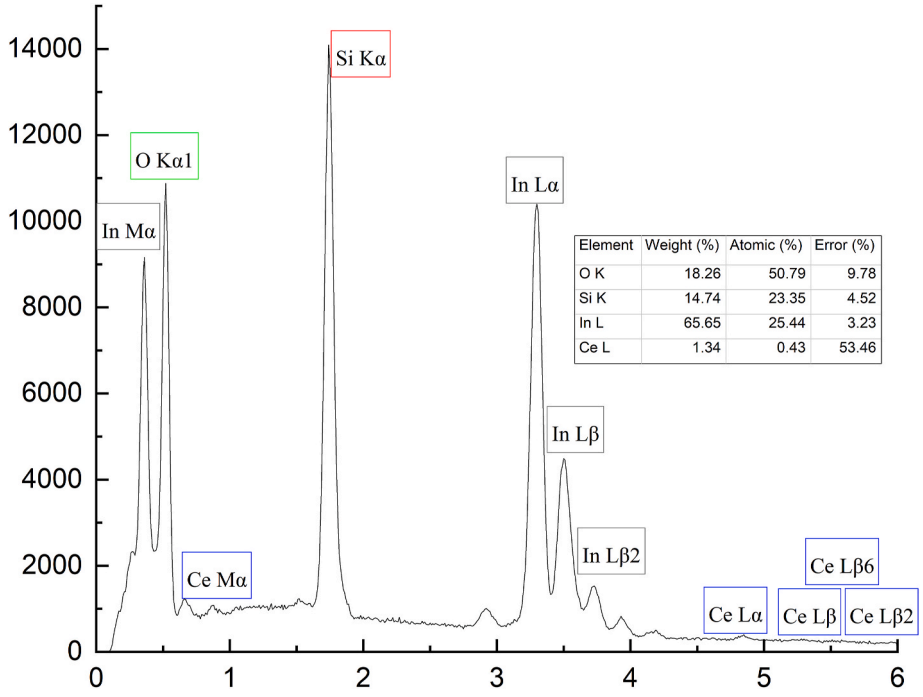

Fig. 8. EDX spectrum of optimized ICO film alongside weight and atomic percentages of elements. Note that the Si peak arises due to Si wafer substrate.

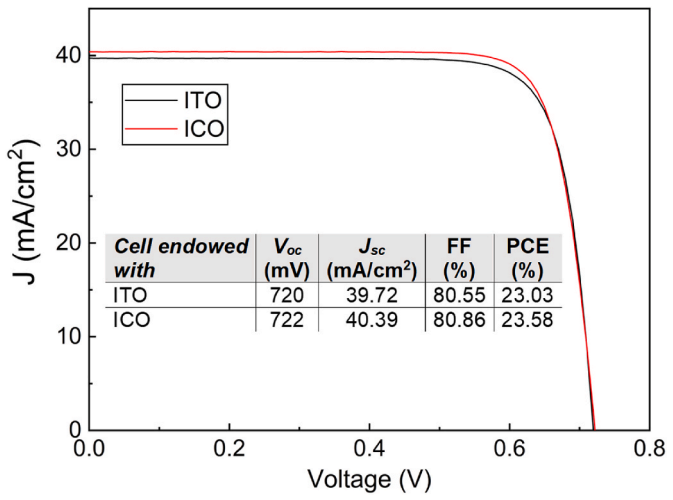

Cell endowed with	V_{oc} (mV)	J_{sc} (mA/cm^2)	FF (%)	PCE (%)
ITO	720	39.72	80.55	23.03
ICO	722	40.39	80.86	23.58

Fig. 9. Comparison in terms of PV external parameters of FBC SHJ solar cells endowed with either developed ICO films or the baseline ITO layers on designated cell area.

and baseline ITO layers are listed in the inset table of Fig. 9. It is demonstrated by both EQE (see Fig. S8) and *J-V* measurements that ICO layers lead to a boost in the J_{SC}. Furthermore, a slightly higher FF could be a sign of lower contact resistivity between the TCO and metal fingers or the ICO and the Si thin-film layers. As a result, implementing ICO layers into FBC-SHJ solar cell architecture yields in an absolute PCE increase of ~0.55 % when compared to the baseline solar cell based on ITO TCO.

4. Conclusions

This work presents the optimization of RF-sputtered ICO thin films, and their application in FBC-SHJ solar cells as a promising TCO layer. Optimized ICO layers deposited at room temperature reached Hall mobility of 44.22 cm^2/Vs, which is more than 56 % higher than that of the ITO reference. The opto-electrical enhancement of our ICO films with respect to the ITO reference layer was reflected at the device level, particularly J_{SC}, with an improvement of 0.67 mA/cm^2 for ICO layers. Fabricated FBC-SHJ solar cells with our optimized layers lead to an absolute increase of PCE's of ~0.55 % when compared to the baseline solar cell with ITO and resulted in ~23.6 % efficiency.

CRediT authorship contribution statement

Engin Özkol: Writing – original draft, Methodology, Formal analysis, Conceptualization. **Maria M.R. Magalhães:** Investigation, Formal analysis. **Yifeng Zhao:** Writing – review & editing, Methodology, Conceptualization. **Liqi Cao:** Investigation, Formal analysis. **Paula Perez-Rodriguez:** Investigation, Formal analysis. **Katarina Kovačević:** Investigation. **Paul Procel:** Writing – review & editing. **Manuel João Mendes:** Supervision, Resources. **Miro Zeman:** Supervision. **Olindo Isabella:** Writing – review & editing, Supervision, Resources.

Declaration of competing interest

The authors declare that they have no known competing financial interests or personal relationships that could have appeared to influence the work reported in this paper.

Acknowledgements

The authors thank the financial support from the *SiLEAN project,* that has received funding from the European Union's Horizon Europe Programme under GA No. 101147275.

Appendix A. Supplementary data

Supplementary data to this article can be found online at https://doi.org/10.1016/j.solmat.2025.113637.

Data availability

Data will be made available on request.

References

[1] H. Wu, F. Ye, M. Yang, et al., Silicon heterojunction back contact solar cells by laser patterning, Nature (2024), https://doi.org/10.1038/s41586-024-08110-8.
[2] A. Richter, M. Hermle, S.W. Glunz, Reassessment of the limiting efficiency for crystalline silicon solar cells, IEEE J. Photovoltaics 3 (4) (2013) 1184–1191, https://doi.org/10.1109/JPHOTOV.2013.2270351.
[3] T. Koida, Y. Ueno, H. Shibata, In2O3-based transparent conducting oxide films with high electron mobility fabricated at low process temperatures, Phys. Status Solidi 215 (7) (2018) 1700506, https://doi.org/10.1002/pssa.201700506.
[4] C. Han, R. Santbergen, M. van Duffelen, P. Procel, Y. Zhao, G. Yang, X. Zhang, M. Zeman, L. Mazzarella, O. Isabella, Towards bifacial silicon heterojunction solar cells with reduced TCO use, Prog. Photovoltaics Res. Appl. 30 (7) (2022) 750–762, https://doi.org/10.1002/pip.3550.
[5] A.B. Morales-Vilches, A. Cruz, S. Pingel, S. Neubert, L. Mazzarella, D. Meza, L. Korte, R. Schlatmann, B. Stannowski, ITO-free silicon heterojunction solar cells with ZnO:Al/SiO2 front electrodes reaching a conversion efficiency of 23%, IEEE J. Photovoltaics 9 (1) (2018) 34–39, https://doi.org/10.1109/JPHOTOV.2018.2873307.
[6] Q. Tang, W. Duan, A. Lambertz, K. Bittkau, M.A. Yaqin, Y. Zhao, K. Zhang, Q. Yang, D. Qiu, F. Gunkel, M. Weber, U. Rau, K. Ding, 85% indium reduction for high-efficiency silicon heterojunction solar cells with aluminum-doped zinc oxide contacts, Sol. Energy Mater. Sol. Cell. 251 (2023) 112120, https://doi.org/10.1016/j.solmat.2022.112120.
[7] F. Jay, T. Gageot, G. Pinoit, B. Thiriot, J. Veirman, R. Cabal, S. De Vecchi, W. Favre, M. Sciuto, C. Gerardi, M. Foti, Reduction in indium usage for silicon heterojunction solar cells in a short-term industrial perspective, Sol. RRL 7 (2023) 2200598, https://doi.org/10.1002/solr.202200598.
[8] B.K. Sarma, P. Rajkumar, Al-doped ZnO transparent conducting oxide with appealing electro-optical properties–Realization of indium free transparent conductors from sputtering targets with varying dopant concentrations, Mater. Today Commun. 23 (2020) 100870, https://doi.org/10.1016/j.mtcomm.2019.100870.
[9] H. Sai, T. Koida, T. Matsui, Improved electrical contact properties in Indium-free silicon heterojunction solar cells with amorphous SnO2 TCO layers, Sol. Energy Mater. Sol. Cell. 278 (2024) 113191, https://doi.org/10.1016/j.solmat.2024.113191.
[10] W. Cui, F. Chen, Y. Li, X. Su, B. Sun, Status and perspectives of transparent conductive oxide films for silicon heterojunction solar cells, Materials Today Nano 22 (2023) 100329, https://doi.org/10.1016/j.mtnano.2023.100329.
[11] J. Wang, C. Meng, L. Zhao, W. Wang, X. Xu, Y. Zhang, H. Yan, Effect of residual water vapor on the performance of indium tin oxide film and silicon heterojunction solar cell, Sol. Energy 204 (2020) 720–725, https://doi.org/10.1016/j.solener.2020.04.086.
[12] E. Kobayashi, Y. Watabe, T. Yamamoto, Y. Yamada, Cerium oxide and hydrogen co-doped indium oxide films for high-efficiency silicon heterojunction solar cells, Sol. Energy Mater. Sol. Cell. 149 (2016) 75–80, https://doi.org/10.1016/j.solmat.2016.01.005.
[13] H. Li, S. Yin, G. Dong, G. Cui, C. Lei, Y. Li, C. Yu, Effect of humidity on optical and electrical properties of Zr-doped In2O3 and a new structure for transparent electrode of silicon heterojunction solar cell, Sol. Energy 196 (2020) 125–131, https://doi.org/10.1016/j.solener.2019.12.017.
[14] M. Morales-Masis, S. De Wolf, R. Woods-Robinson, J.W. Ager, C. Ballif, Transparent electrodes for efficient optoelectronics, Advanced Electronic Materials 3 (5) (2017) 1600529, https://doi.org/10.1002/aelm.201600529.
[15] H. Liu, Y. Gong, H. Diao, et al., Comparative study on IWO and ICO transparent conductive oxide films prepared by reactive plasma deposition for copper electroplated silicon heterojunction solar cell, J. Mater. Sci. Mater. Electron. 33 (2022) 5000–5008, https://doi.org/10.1007/s10854-021-07689-2.
[16] J. Nomoto, T. Koida, I. Yamaguchi, et al., Over 130 cm2/Vs Hall mobility of flexible transparent conductive In2O3 films by excimer-laser solid-phase crystallization, NPG Asia Mater. 14 (2022) 76, https://doi.org/10.1038/s41427-022-00421-4.
[17] J. Shi, F. Meng, J. Bao, Y. Liu, Z. Liu, Surface scattering effect on the electrical mobility of ultrathin Ce doped In2O3 film prepared at low temperature, Mater. Lett. 225 (2018) 54–56, https://doi.org/10.1016/j.matlet.2018.04.102.
[18] Z. Gao, C. Han, J. Pan, J. Shen, Z. Liu, K. Chen, Z. Yi, Y. Zhang, Z. Yu, X. Zhou, P. Gao, Source material design for realizing >50% indium-saving transparent electrode toward sustainable development of silicon heterojunction solar cells, ACS Appl. Mater. Interfaces 17 (2) (2025) 3265–3277, https://doi.org/10.1021/acsami.4c15684.

[19] H. Lin, M. Yang, X. Ru, et al., Silicon heterojunction solar cells with up to 26.81% efficiency achieved by electrically optimized nanocrystalline-silicon hole contact layers, Nat. Energy 8 (2023) 789–799, https://doi.org/10.1038/s41560-023-01255-2.

[20] A. Cruz, D. Erfurt, R. Köhler, M. Dimer, E. Schneiderlöchner, B. Stannowski, Industrial TCOs for SHJ solar cells: approaches for optimizing performance and cost. Photovoltaics International, 44th ed., Solar Media Limited, London, UK, 2020, p. 86.

[21] L. Tutsch, H. Sai, et al., The sputter deposition of broadband transparent and highly conductive cerium and hydrogen co-doped indium oxide and its transfer to silicon heterojunction solar cells, Prog. Photovoltaics Res. Appl. 29 (2021) 835–845, https://doi.org/10.1002/pip.3388.

[22] S. An, P. Chen, F. Hou, Q. Wang, H. Pan, X. Chen, X. Lu, Y. Zhao, Q. Huang, X. Zhang, Cerium-doped indium oxide transparent electrode for semi-transparent perovskite and perovskite/silicon tandem solar cells, Sol. Energy 196 (2020) 409, https://doi.org/10.1016/j.solener.2019.12.040.

[23] E. Özkol, P. Wagner, F. Ruske, B. Stannowski, L. Korte, Optimization of silicon heterojunction interface passivation on p- and n-type wafers using optical emission spectroscopy, Phys. Status Solidi A 219 (2022) 2100511, https://doi.org/10.1002/pssa.202100511.

[24] C. Han, Y. Zhao, L. Mazzarella, R. Santbergen, A. Montes, P. Procel, O. Isabella, Room-temperature sputtered tungsten-doped indium oxide for improved current in silicon heterojunction solar cells, Sol. Energy Mater. Sol. Cell. 227 (2021) 111082, https://doi.org/10.1016/j.solmat.2021.111082.

[25] V. Assunção, E. Fortunato, A. Marques, H. Águas, I. Ferreira, M. Costa, R. Martins, Influence of the deposition pressure on the properties of transparent and conductive ZnO:Ga thin-film produced by r.f. sputtering at room temperature, Thin Solid Films 427 (1–2) (2003) 401–405, https://doi.org/10.1016/S0040-6090(02)01184-7.

[26] S.P. Harvey, et al., Surface versus bulk electronic/defect structures of transparent conducting oxides: I. Indium oxide and ITO, J. Phys. D Appl. Phys. 39 (2006) 3959, https://doi.org/10.1088/0022-3727/39/18/006.

[27] A.P. Amalathas, M.M. Alkaisi, Effects of film thickness and sputtering power on properties of ITO thin films deposited by RF magnetron sputtering without oxygen, J. Mater. Sci. Mater. Electron. 27 (2016) 11064–11071, https://doi.org/10.1007/s10854-016-5223-9.

[28] Y. Zhao, P. Procel, C. Han, L. Cao, G. Yang, E. Özkol, A. Alcañiz, K. Kovačević, G. Limodio, R. Santbergen, A. Smets, A. Weeber, M. Zeman, L. Mazzarella, O. Isabella, Strategies for realizing high-efficiency silicon heterojunction solar cells, Sol. Energy Mater. Sol. Cell. 258 (2023) 112413, https://doi.org/10.1016/j.solmat.2023.112413.